

# PREDICTION OF EROSION INDUCED BY SOLID PARTICLES IN A WATER TURBINE

*Adel Ghenaiet*

Faculty of Mechanical Engineering, University of Sciences and Technology, USTHB,  
BP32 El-Alia, 16111, Algiers, Algeria, Email: ag1964@yahoo.com

## ABSTRACT

Erosion is one of the major problems that restricts the lifetime of hydraulic turbines, especially the parts exposed to higher flow velocities. This paper presents a numerical simulation of erosion by solid particles entrained by the water flow through the components of a small Francis turbine. The computation of particle trajectories used our developed Lagrangian tracking code that considers random particle size and shape distribution and the effects of turbulence and near wall as well as the stator/rotor relative positions. As the impacts were predicted, a semi empirical erosion model was used to assess the mass erosion and the geometry degradation. The nature of the flow field in the runner of the investigated Francis turbine leads to a fluid-particle interaction more complex and strongly affecting the erosion patterns. The obtained results allow identifying the critical areas of erosion wear, where surfaces coatings are necessary to increase the lifetime for these sand laden water turbines.

## NOMENCLATURE

$A_e$	Area of a surface element		Greek letters
$C_D$	Drag coefficient	$\beta$	Impact angle (deg)
$C_L$	Lift coefficient	$\varepsilon$	Erosion rate (mg/g)
$d$	Diameter	$\mu$	Dynamic viscosity (kg/m.s)
$E_q$	Equivalent erosion rate (mg/g/mm <sup>2</sup> )	$\rho$	Density (kg/m <sup>3</sup> )
$F_b$	Buoyancy force	$\omega$	Speed of rotation (rd/s)
$F_D$	Drag force	$\theta$	Tangential co-ordinate
$F_S$	Saffman force		Subscript
$g$	Gravity	$i$	Impact
$m$	Mass	$n$	Normal
$r$	Radius, radial co-ordinate	$p$	Particle
$Re$	Reynolds number	$r$	Radial
$t$	Time	$s$	Shear
$V_f$	Fluid velocity	$\theta$	Tangential
$V_p$	Particle velocity	$z$	Axial
$z$	Axial co-ordinate	$1, 2$	At impact and rebound

## INTRODUCTION

The erosion problem is particularly important during rainy seasons due to infiltration of high number of solid particles to the hydroelectric power plants where an exhaustive filtration is not available. The issue of sand erosion is equally important for the operation and the maintenance of hydropower plants. This latter is one of the major problems that restricts the lifetime of water turbines (Francis turbines), and their efficiency decreases as being damaged by erosion processes, especially the parts exposed to high flow velocities. Erosive wear is a complex phenomenon that

depends upon different parameters, such as the number of particles, particle size and hardness, velocity of water, impacting conditions and the base material properties. In general, where the flow direction changes rapidly such as the case of the turbine blades, the induced erosion is usually more severe because the particle motion is governed by the local flow patterns that change significantly. The development of erosion prediction models used in turbomachinery began with some experiments to obtain the basic erosion data. Sage and Tilly [1] were among the early researchers who attempted to quantify the erosion effects in turbomachinery. Since the report made by Truscott [2], erosion of turbomachinery had been investigated over the past decades. Hussein and Tabakoff [3] pioneered in the simulations of particle trajectories through the axial turbomachinery and in the use of experimentally based particle restitution factors. Later, the particle trajectories and erosion in radial turbomachinery were shown to be consistently different from those of axial turbomachinery, owing to the flow complexity and the direction of centrifugal forces as reported by Elfeki and Tabakoff [4] and Ghenaïet [5]. According to Tabakoff and Hamed [6], in a radial turbine the high erosion rates are induced by large number of particles consistently impacting a smaller area on the rotor pressure side, due to the high centrifugal force and the flow direction. The present paper is aimed at studying the solid particle trajectories through the components of a small Francis turbine and the subsequent erosion wear, based on our in-house Lagrangian tracking code [5, 7-9]. The details of the flow field around the vanes and the runner revealed the formation of strong entrance and bend vortices that resulted in a complex fluid-particle interaction. The local impingement conditions were quantified in order to determine the areas susceptible to particle impacts and frequency as well as the assessment of local metal loss rates. The erosion distributions in the vane and the runner allowed identifying the areas of wear and the critical regions where a special surface coat is necessary in order to prevent risk of erosion and to increase the lifetime of these components.

## CFD INVESTIGATION

This small Francis turbine taken from a hydraulic test bench encompasses a volute, a distributor with 6 adjustable vanes with an opening angle of maximum 9 deg with respect to tangential direction and a runner with 10 fixed blades made from stainless steel. The other data are: inlet diameter of spiral case of 38 mm, outlet diameter of spiral case of 149 mm, vane height of 8 mm, runner inlet and outlet diameter of 83 mm and 38 mm, respectively and a draft tube outlet diameter of 80 mm. The CAD model of this Francis turbine used a 3D tri-optic measuring machine. The flow field was solved using the commercial code CFX. The full passageway between the inlet from the spiral case side and the outlet of draft tube side is depicted by Fig. 1. For the computational domain, structured 3D hexahedral meshing was generated in CFX-Turbogrid for the vane and rotor as shown by Fig. 2, and with Gambit for the volute and the draft pipe. A fine meshing is used around vane and rotor blade, the leading and trailing edge and near the hub and shroud, and near the walls of volute and draft pipe. A mesh dependency study allowed taking 3550490 nodes for the complete computational domain consisting of a volute full vanes and rotor blades and a draft pipe, was used for the CFD Hydrodynamic performance simulations, whereas a domain of mesh size 874434 nodes consisting of one vane, one rotor blade and a sector of draft pipe was used in particle trajectory computations. As far as the quality of the mesh is concerned, some parameters have to be checked such as skew angles between 15°-120°, the minimum positive volumes and the aspect ratios not more than 100. To reduce the resolution requirements an automatic wall treatment is implemented. The near wall nodes are positioned in such a way that  $y^+ = \rho y_p u_t / \mu$  ( $u_t = V_\infty \sqrt{0.5 C_f}$ , and  $V_\infty$  is flow velocity). The friction factor  $C_f = 0.027 Re_x^{-\frac{1}{4}}$  is based on a flat plate, which the average values are based on vane and rotor blade chord lengths. For volute and draft pipe a hydraulic diameter is used for the friction coefficient. In order to cover regions of high Reynolds number, the maximum flow velocity and density and minimum dynamic viscosity are used. Figure 3 depicts values of  $y^+$  over the surfaces of vanes and rotor blades, of maximum values essentially around the trailing edge of vane and leading edge of rotor, but not exceeding 31.6.

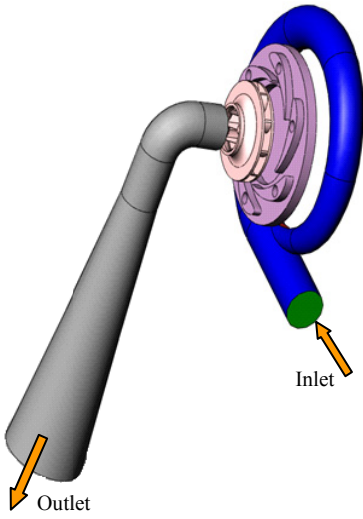


Figure 1. CAD views

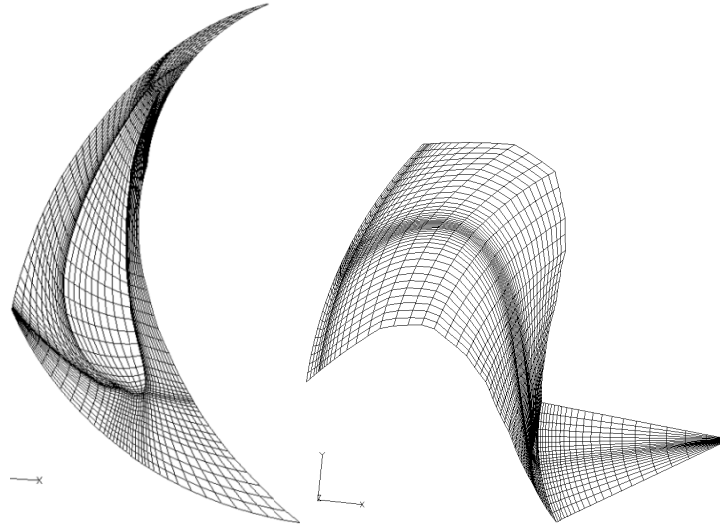


Figure 2. Grids: left) Vane grid, right) Rotor grid

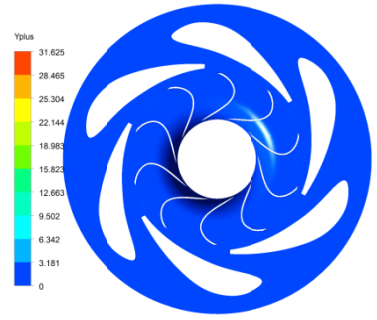


Figure 3.  $y^+$  values

The appropriate boundary conditions for this Francis turbine are an imposed mass flow rate specified at the inlet of spiral casing, and an opening condition at the outlet of draft pipe exit with an atmospheric pressure imposed. The periodic boundaries are applied at one pitch away from the vane and the rotor blade, in order to reduce the overall size of the computational domain. The averaged Navier Stokes equations are discretized by the finite volume method in the spatial direction. A turbulence model  $k-\omega$  based SST with automatic wall functions was selected as it is well adapted in regions with large normal strains like the stagnation and regions with strong flow acceleration. First, the flow computations were carried out for the frozen rotor interface using a local time step, and the results were used for the flow simulations considering the stage interface to obtain the hydrodynamic characteristics of this turbine.

Figure 4 presents the comparison between the CFD and the experimental results (dashed line) for the characteristics of power produced, performed for the optimum points corresponding to each rotating speed. It can be readily observed that for the optimum loading the accuracy in the CFD prediction is deemed satisfactory. Figure 5 presents the predicted hydrodynamic characteristics, depicting that the produced power increases with the volume flow rate at different rotational speeds. For the speed of 2360 rpm, the power sweeping the whole operation range is 470 W, that becomes only 124 W for the rotational speed of 1100 rpm. Also, the flow rate of 165 l/min at the rotational speed of 1900 rpm is shown to correspond to the optimum operating point, for an efficiency reaching a maximum value of 79.18 %.

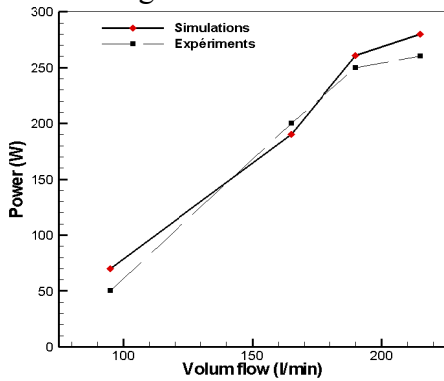


Figure 4. Power simulated and tested

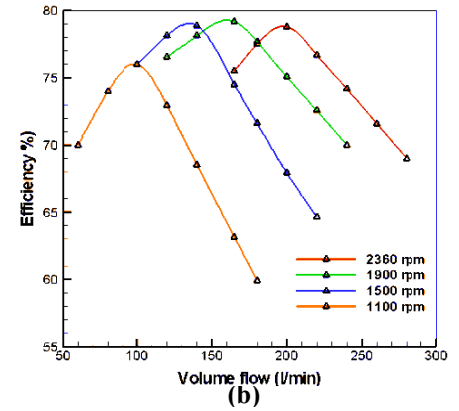
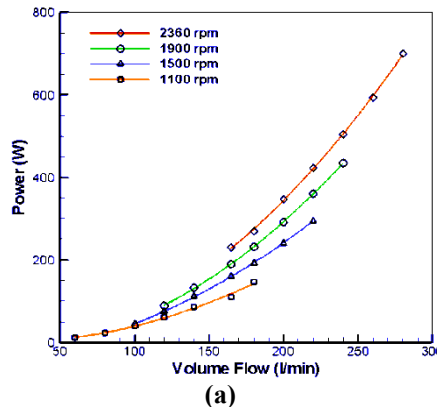
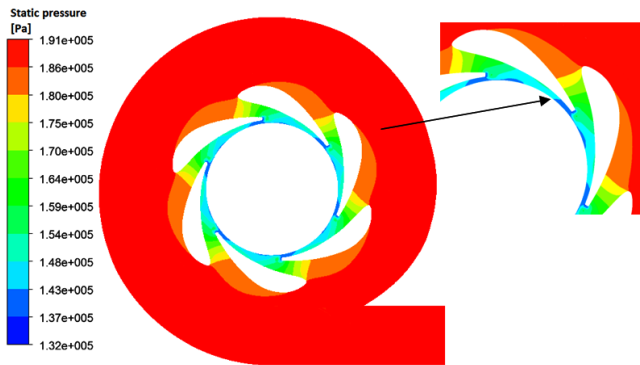


Figure 1. Hydrodynamic characteristics: a) Produced power, b) Efficiency

For the CFD and particles trajectories results analyses, the optimum operating point (i.e. flow rate of 165 l/s at the rotational speed of 1900 rpm) was used. For this investigated point, the value of static pressure at inlet of spiral case was  $1.91 \times 10^5$  kPa. As seen from Fig. 6, the static pressure

drops along the vane and runner where it reaches the lowest depression beyond the throat towards the tip of exducer. The level of static pressure is recovered to its atmospheric value at the exit from the draft pipe. Figure 7 plots the flow velocity contours in the volute and vane. The stagnation region is seen to be shifted from the leading edge over the suction side of vane. The flow is accelerated starting from the first third of pressure side, whereas over the suction side it is beyond the last third, and reaches the highest flow velocity at exit. In the runner, the flow velocities are lower as compared to the vane, but there is an acceleration seen beyond the throat because of the reaction design for this type of hydraulic turbine. A large eddy (Fig. 8) develops over the large part of the pressure side, extending to nearly 60 % of meridional distance, which is clearer from streamlines plots in Fig. 9. There is also a clear vortex caused by the high negative incidence of the flow at entrance. At the runner exit and near the hub there is another eddy formed, which mixes with the impinging jet water from the exducer. The flow velocities contours at mid-span and near shroud (Fig. 10a-b) show a vortex originating at the blade leading edge caused by the large incidence and a large eddy extending over the runner pressure side from hub to shroud. The flow at the rotor entrance is arriving at a high tangential velocity component with a small relative eddy caused by the flow on the pressure side that moves in the opposite direction to the bulk of flow. The pressure side vortex tends to push the inlet flow out and up away from the hub and shroud pressure side corner. Near the blade surface near tip, the flow is already being turned to follow the blade direction as the incidence becomes lower. Also there is an evidence of two counter rotating vortices, where the second is seen to develop towards the suction side as well. The cross section at mid channel reveals that the second vortex reaches the suction side and the flow is not aligned with the blade. The intensity of the first vortex reduces but develops into corner vortices one near the hub and another near the shroud. Near the hub pressure corner there are very low velocities as the bulk of flow swings around this stagnation region, resulting in a lack of work transfer. Near the throat of rotor blade, the suction side secondary flow is getting stronger and being continually fed by the jet pushing into the hub pressure corner and upward to produce a severe under-turning in the top of blade. At exit most of the passage is at high flow velocities particularly near the pressure side where the secondary flow is being restricted to the top third of blade.



**Figure 6.** Static pressure at mid-span of volute and vane

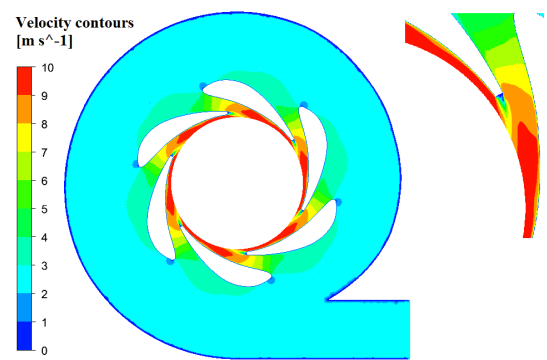


**Figure 7.** Velocity contours at mid-span of volute and vane

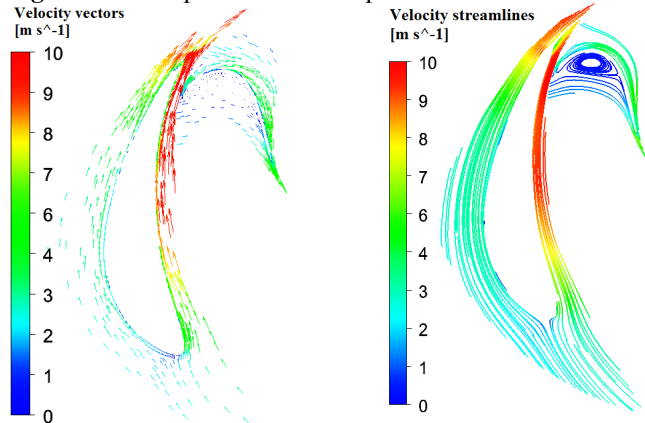


**Figure 8.** Velocity vectors

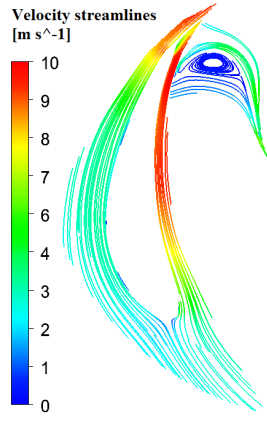


**Figure 9.** Streamlines

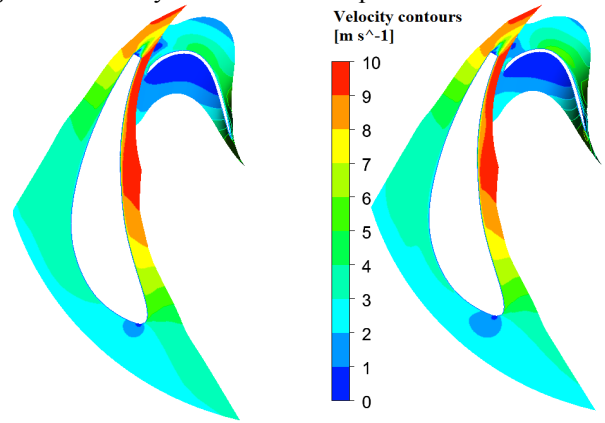


**Figure 10.** Velocity contours: a) 50% span, b) 90% span

## PARTICLES TRAJECTORIES

The Eulerian approach considers the flow and solid phases as separate interpenetrating continua where the conventional time averaged transport equations are solved to predict the field distributions of the momentum and volume fraction of each phase. Such an approach is preferably used for dense two-phase flows [10]. The Lagrangian approach treats the dispersed phase separately by solving the equations of particle trajectories and tracking a large number of individual trajectories from different starting positions to achieve a stochastically significant solution [11]. This approach is preferred in predicting erosion of turbomachinery, since the effect of particle phase on the flow solution can be neglected as the volume fraction is often less than the upper limit of  $10^{-6}$  [12], and also because of its relative ease in implementation and high level of information regarding the impact conditions at a wall. The particle trajectory equations are derived from the intuitive superposition of various involved forces, but in most particulate flows the drag force is dominant. The general drag expression for the drag coefficient is given as below according to Haider and Levenspiel [13], valid for Reynolds number from 0.01 to  $2.6 \times 10^5$ . Above this value the drag coefficient falls sharply to a value of approximately 0.1 at  $Re = 3 \times 10^5$  and again rises slowly with the Reynolds number past this point, and the standard drag curve is used. The constants  $A$ ,  $B$ ,  $C$  and  $D$  depend on the particle shape. For small Reynolds numbers  $Re < 0.5$  the viscous effect is dominating and this is referred as the Stokes regime  $C_D = 24/Re$  and this value is used at very low Reynolds number.

$$\vec{F}_D = \frac{\pi}{8} d_p^2 \rho_f C_D (\vec{V}_f - \vec{V}_p) \|\vec{V}_f - \vec{V}_p\| \quad , \quad C_D = \frac{24}{Re_p} (1 + A Re_p^B) + C / (1 + D / Re_p) \quad , \quad Re_p = \frac{\rho_f}{\mu_f} d_p \|\vec{V}_f - \vec{V}_p\| \quad (1)$$

During the computations the Reynolds number varied from 0.146 to 2486.27 for small particles of  $5 \mu m$ , whereas for large ones such as  $1000 \mu m$  the Reynolds number varied from 467.6 to 436684.5

If a particle is sufficiently large and there is a large velocity gradient, there will be a particle lifting force called Saffman force due to fluid shearing forces [10], which depends on the particle based Reynolds number and the shear flow Reynolds number [12] as follows.

$$\vec{F}_S = \frac{\rho_f \pi}{8} d_p^3 C_{LS} (\vec{V}_f - \vec{V}_p) \times \nabla \vec{V}_f \quad , \quad C_{LS} = \frac{4.1126}{\sqrt{Re_s}} f(Re_p, Re_s) \quad , \quad Re_s = \frac{\rho_f}{\mu_f} d_p^2 |\vec{\omega}_f| \quad (2)$$

The buoyancy force is also considered for the case of water.

$$\vec{F}_b = \frac{\pi}{6} d_p^3 (\rho_p - \rho_f) \vec{g} \quad (3)$$

As a particle approaches a wall it must pass through a layer of water, and the fluid between wall and particle must be displaced to allow the particle impinging the wall. The squeeze film model of Clark and Burmeister [14] depends primarily on the particle Reynolds number, which when exceeding a critical value; the particle will possess a sufficient momentum to penetrate the squeeze film and thus impinges the wall. As a particle penetrates this film its normal velocity reduces by a certain factor. The turbulent effect on a particle motion depends on the instantaneous flow velocity components of a particular eddy determined from the local turbulence properties. This effect is assumed to prevail as long as the particle-eddy interaction time is lower than the eddy lifetime and its displacement relative to an eddy does not exceed the eddy length, Gosman and Ioannides [15].

The set of second order non-linear differential equations of solid particle motion as derived in the rotating frame is resulting in centrifugal and Coriolis forces.

$$\begin{cases} \frac{d^2 r_p}{dt^2} = \frac{3\rho_f C_D}{4\rho_p d_p} \sqrt{|V_{fr} - V_{pr}|^2 + |V_{f\theta} - V_{p\theta}|^2 + |V_{fz} - V_{pz}|^2} \left( V_{fr} - \frac{dr_p}{dt} \right) + r_p \left( \omega + \frac{d\theta_p}{dt} \right)^2 + \left( 1 - \frac{\rho_f}{\rho_p} \right) g \sin \theta_p + \frac{F_{Sr}}{m_p} \\ r_p \frac{d^2 \theta_p}{dt^2} = \frac{3\rho_f C_D}{4\rho_p d_p} \sqrt{|V_{fr} - V_{pr}|^2 + |V_{f\theta} - V_{p\theta}|^2 + |V_{fz} - V_{pz}|^2} \left( V_{f\theta} - \frac{d(r_p \theta_p)}{dt} \right) - 2 \frac{dr_p}{dt} \left( \omega + \frac{d\theta_p}{dt} \right) + \left( 1 - \frac{\rho_f}{\rho_p} \right) g \cos \theta_p + \frac{F_{S\theta}}{m_p} \\ \frac{d^2 z_p}{dt^2} = \frac{3\rho_f C_D}{4\rho_p d_p} \sqrt{|V_{fr} - V_{pr}|^2 + |V_{f\theta} - V_{p\theta}|^2 + |V_{fz} - V_{pz}|^2} \left( V_{fz} - \frac{dz_p}{dt} \right) + \frac{F_{Sz}}{m_p} \end{cases} \quad (4)$$

In this Lagrangian approach the system of equations (4) is solved and the individual trajectories of particles are tracked from their starting positions. Particle tracking through the computational

cells requires transforming each particle position its physical co-ordinates into local co-ordinates by solving a set of non-linear equations and updating its position in a new cell if a local value exceeds the value unity. The flow field data at the representative mesh points are used to interpolate the flow properties during the integration of particle trajectories by Runge-Kutta-Fehlberg seventh order technique [16]. For a good convergence, the integration time step is estimated based on the sizes of computational cells and flow velocities and rotational speed. However, this latter is reduced within the integration to keep the leading truncation error term within the prescribed tolerance. If a particle interacts with an eddy, the interaction time is considered as the effective time step. Near a boundary condition the particle is moved back and a more accurate time step is re-evaluated from a non-linear equation to get an impact within half diameter distance. The considered boundary conditions are: Periodic boundary conditions at the lateral sides of all domains. At an interface plane between a stationary and a rotating frame, the particle velocity is decomposed into a peripheral and a relative velocity. At a point of impact, the rebound velocity and angle are computed statistically based on the values of mean and standard deviation of the rebound factors derived experimentally by Tabakoff et al. [17] given as polynomial regressions equation (5). At a point of impact each particle fragments and the new diameter is used.

$$V_{P2}/V_{P1} = \sum_{i=0}^4 a_i \beta_i^i \quad , \quad \beta_{P2}/\beta_{P1} = \sum_{i=0}^4 b_i \beta_i^i \quad (5)$$

The particles trajectories were simulated through this Francis turbine when operating at a flow rate of 165 l/min and a rotational speed of 1900 rpm. The number of seeded particles and their initial positions were estimated based on the sand (quartz) particle size distribution (0-1000 $\mu$ m) and the given mid to high concentrations from 50 to 1000 mg/m<sup>3</sup>. Iterations on the number of particles and sizes were repeated till reaching the convergence in the total mass of particles.

## EROSION ASSESSMENT

Finnie [18] attempted to predict the erosion rate as being directly proportional to the particle kinetic energy and inversely to the minimum flow stress of the target material. Goodwin et al [19] correlated the erosion rate against the hardness of erodent. Rao and Buckley [20] provided a useful correlation between erosion rate and material properties such as hardness, strain energy and melting point. The most successful erosion prediction equation directly applied to turbomachinery is that due to Grant and Tabakoff [21], who revealed that the erosion process depends on two mechanisms; one predominant at low impact angle and the other at high impact angle. The first part of equation 6 is related to the tangential velocity component which does the cutting action while the normal velocity component (second part) contributes for the deformation. Ball and Tabakoff [22] extended Grant and Tabakoff correlation to steel alloys based on a similar expression, but with modified constants.

$$E = K_1 f(\beta_1) (V_{1\theta}^2 - V_{2\theta}^2) + f(V_{1N}) \quad (6)$$

Erosion evaluation depends on the local flow conditions, material and geometry of blades, number of particles striking a surface and the velocity and direction which have to be determined and used in the calculation of erosion rates. The values of mass erosion in *mg* are calculated from the local erosion rates according to equation 6, and then cumulated on the meshes' faces and used to compute the equivalent erosion levels in *mg/g/cm<sup>2</sup>*.

$$E_q = \frac{1}{A_e \sum_{i=1}^N m_{p_i}} \sum_{i=1}^N m_{p_i} \varepsilon_i \quad (7)$$

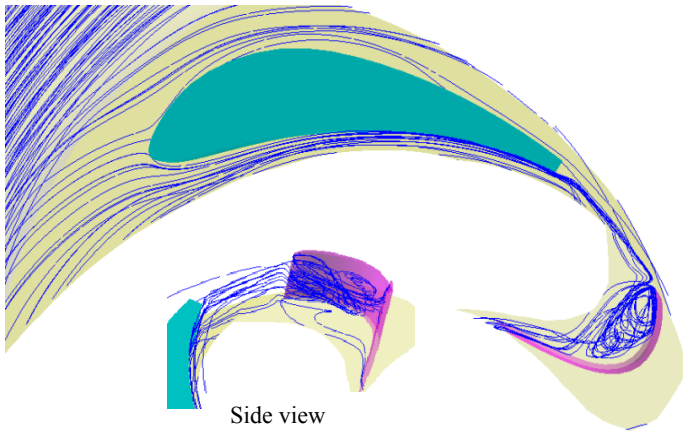
## RESULTS AND DISCUSSION

The sand particles as released in the intake tend to follow different trajectories depending on their sizes. Figures 10, 13 and 16 are presenting samples of trajectories for particle size 25 $\mu$ m, 100  $\mu$ m and 1000  $\mu$ m, through one vane and one rotor blade passage. Small size particles such as 25  $\mu$ m tend to follow flow streamlines (Fig. 11) and are strongly influenced by the turbulence effect and

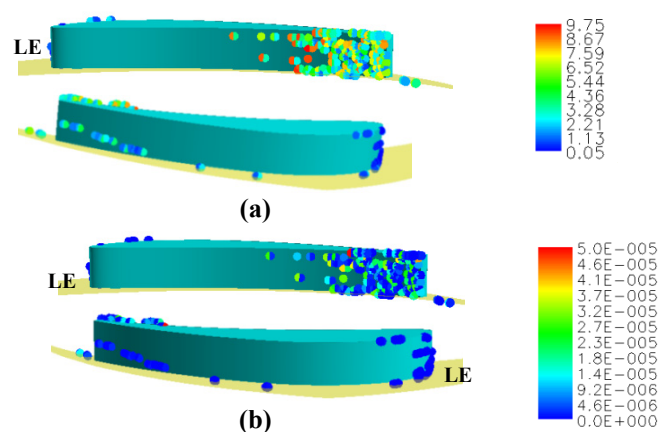
the secondary flows. Figure 12.a shows that these particles impact the leading edge of vane practically from hub to shroud. The main flux of these particles is seen to hit the last third of pressure side and tend to collect at high frequency of impacts beyond the throat till the trailing edge where they are accelerated by the high exit flow velocity. Over the suction side, there are few impacts over the fore part, and particles are deviated upward when approaching the trailing edge. Figure 12.a depicts that the local velocity of impacts are reaching only a value of 9.75 m/s, which is low when compared to that encountered in a gas turbine's NGV [9]. As a result the local rates of erosion (Figure 12.b) are very low and have a maximum of  $5 \times 10^{-5}$  mg/g which is very low as compared with gas turbines [9]. After exiting the vane, the particles enter the rotor with respect to the rotating frame (Fig. 11), where they arrive at relatively different directions to the runner leading edge. The common depicted feature is that these small particles stick to the flow path, and tend to follow the large eddy formed along the pressure side and circle within it several times. Some of these particles escape and may reach the last part of runner and exit after acquiring a sufficient kinetic energy. Moreover, many other particles are seen to cross the runner without interacting with the eddy and afterward impact the third part of pressure side around the throat. As evidence, a flux of particles is extremely deviated around the suction side and only few of these small sand particles may encounter this side. A sample of impacts is well illustrated by Fig. 13, revealing the main impacted areas over the pressure side of blade begging from the entrance, characterized by low impact velocities as compared to a gas turbine's rotor [9]. The next area impacted with a higher velocity up to 5.4 m/s is visible beyond the bend of blade, expending mainly over the second half of blade span till the exit. The impacts over suction side are mainly concentrated towards the exit top corner. The subsequent erosion rates are less than in the vane owing to the low impact velocities. The maximum erosion is revealed towards the top corner from the blade exit. The trajectories of larger sand particles of size 100  $\mu\text{m}$  (Fig. 14) are seen to deviate from the flow streamlines when crossing the vane, and some of them impact at the fore of suction side and deviate considerably due to inertia. On the other side, several of these particles are hit along the leading edge and bounce to impact repeatedly beyond the second half of vane pressure side. The majority of particles are shown (Fig. 14) to reach the second half of vane and do impacts with a velocity up to 10.5 m/s which is reduced by multiple bounces, and then tend to collect towards the trailing edge in a sort of a dense flux of particles accelerated by the efflux flow velocity. At the entry of rotor blade this dense flux of particles split into two parts (Fig. 14), the first after hitting the leading edge of blade is deviated away from the suction side, whereas second part particles, due to the large drag exerted on them tend to follow the formed eddy and cycle within. Some of particles pass without interacting with this eddy and hit the pressure side at the exit. The sample of incurred impacts (Fig. 15.a) reveal a main area seen at the fore part of blade pressure side from entrance, as impacted at low velocities, and subsequently the erosion rates (Fig. 15.b) are very low compared to gas turbines. In addition, there are only few impacts on the hub. Very large sand particles such as size 1000  $\mu\text{m}$ , as depicted by Fig. 17, tend to follow ballistic trajectories due to their high inertia. Many of these particles after impacting the suction side of vane near leading edge bounce off and deviate noticeably in a parabola trajectory to reach the next blade at its leading edge, whereas some impact repeatedly over the opposite pressure side from the second half of blade. In addition, the particles after striking the leading edge are forced to reach the second half of pressure side at relatively high impact velocities about 10.7 m/s (Fig. 18.a), and bounce at low angles of impingement. The process of impaction is repeated several times by quasi straight trajectories (Fig. 17) to reach the trailing edge of blade, where particles collect in a sort of a dense flux deflected upward, resulting in a subsequent eroded area at relatively higher erosion rates, as seen from Fig. 18.b. At the interface plane, these large particles enter the runner at different paths' directions (Fig. 17) and strike the leading edge of blade and over the fore part of suction side, after bouncing even twice they deviate in a bow shaped trajectories and centrifuged back due to the effect of inertia and drag forces. The majority of them after going inward reverses their direction under the influence of the centrifugal and drag force and particles are unable to go further through the runner passage. As a result and according to Figs.



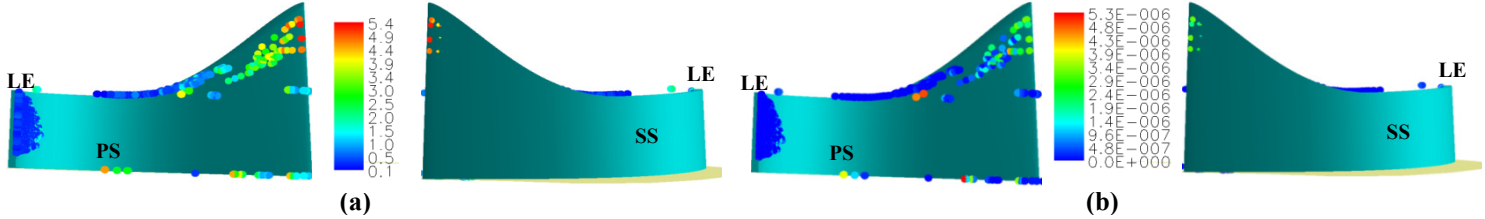
19.a-b, the pressure side and suction side have few impacts characterized by low rates of erosion. The impacts seen near shroud are due particles entrained near the shroud where the pressure level is lowest. When sand particles of different sizes, randomly distributed (10-1000  $\mu\text{m}$ ), are injected upstream the spiral case, the trajectories and locations of impactions are extremely dependent on the particle size. The trajectories trends can be related to the particle momentum Stokes number defined as the ratio of the particle response time to a characteristic time scale of the flow. Indeed, the particles with a Stokes number below 0.1 generally follow the streamlines, and those with Stokes number beyond 10 generally impact on the surfaces of vane and blade, whereas those typically with higher Stokes numbers tend to impact the surfaces via ballistic impactions. According to Fig. 20, the majority of particles are shown to impact the second half of blade pressure side with velocities up to 10.9 m/s. In addition, some of them are shown to impact the leading edge of vane as well as a narrow strip over suction side but with lower velocities. The subsequent local rates of erosion are plotted in Fig. 20.c, showing higher rates visible on pressure side beyond the throat till the trailing edge at upward. As the particles cross the runner, several particles of sizes below 250  $\mu\text{m}$  are seen to impact the blade pressure side from entrance (Fig. 21.a) with low velocities (Fig. 21.b) and subsequently the local erosion rates are very low (Fig. 21.c) as compared to the values encountered in gas turbines [9]. Also, it is clear that the suction side is exempt from impacts.



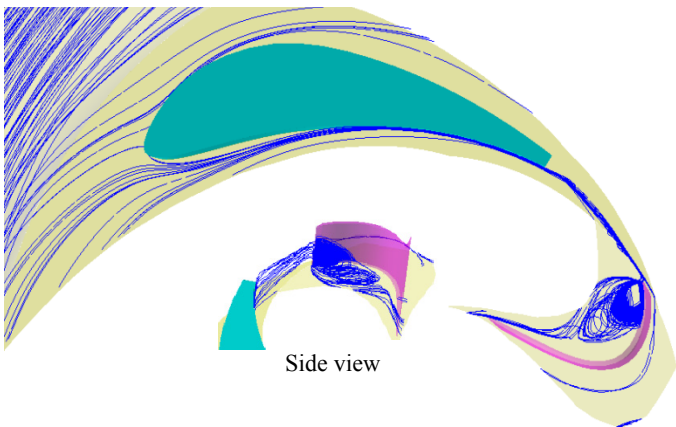
**Figure 11.** Sample of trajectories in vane and rotor for sand particle 25  $\mu\text{m}$ , operating at 1900 rpm



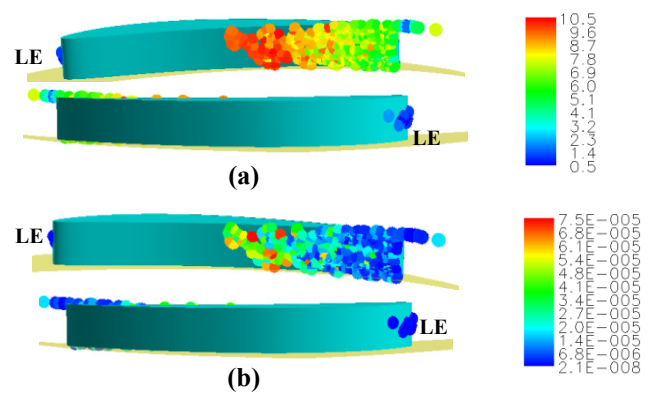
**Figure 12.** Sample of impacts over the vane with particles 25  $\mu\text{m}$ , a) Impact velocity (m/s), b) Local erosion (mg/g)



**Figure 13.** Sample of local impacts over the blade with particles 25  $\mu\text{m}$ , a) Impact velocity (m/s), b) erosion rates (mg/g)

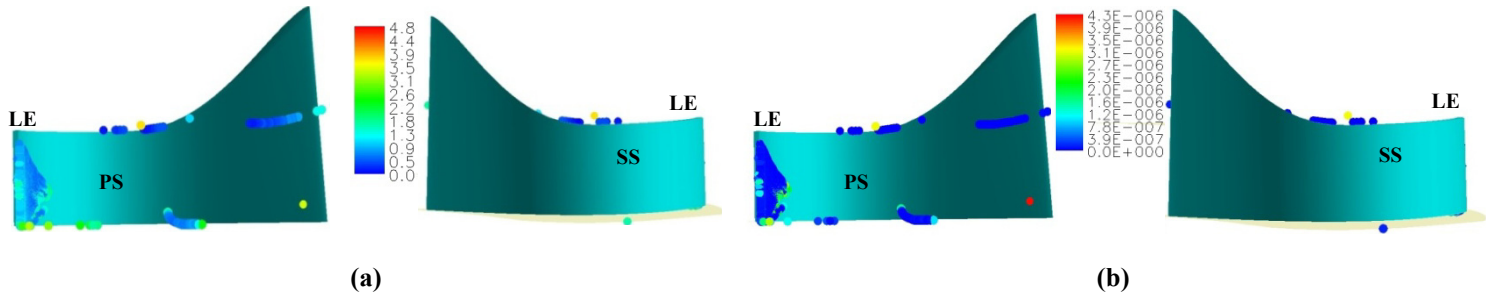


**Figure 14.** Sample of trajectories in vane and rotor for sand particle 100  $\mu\text{m}$ , when operating at 1900 rpm

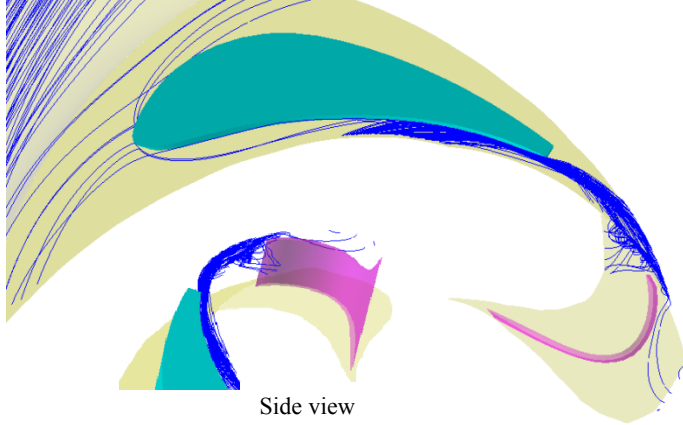


**Figure 15.** Sample of impacts over the vane, particles 100  $\mu\text{m}$ : a) Impact velocity (m/s), b) Local erosion (mg/g)

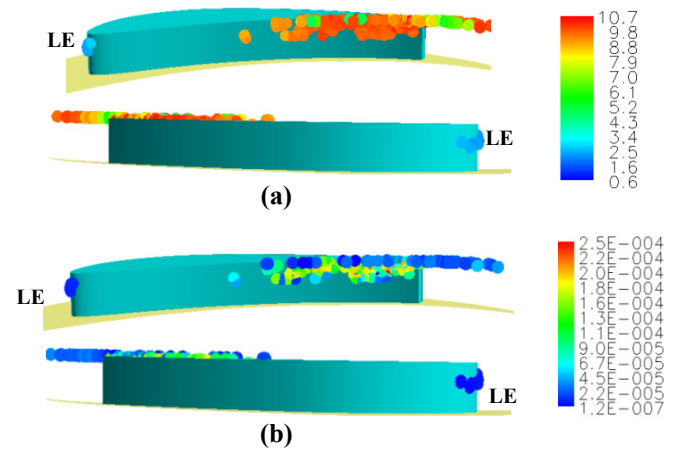




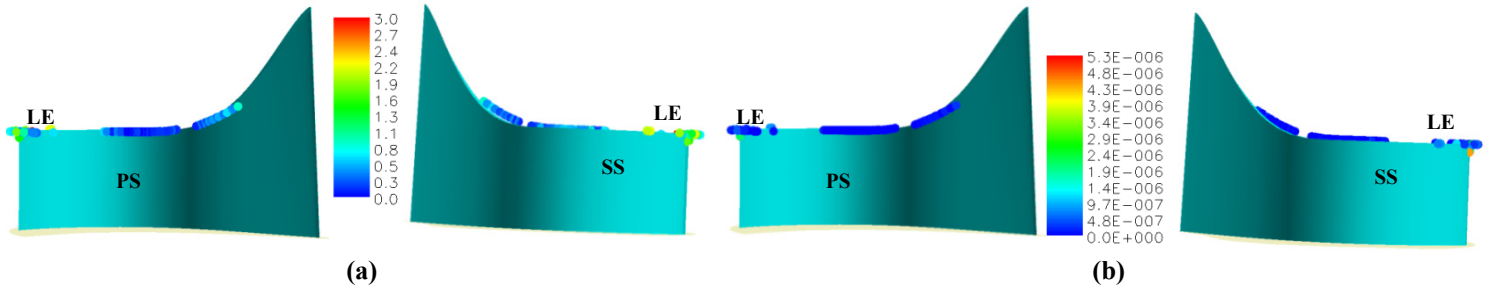
**Figure 16.** Sample of impacts over the rotor blade with particles 100  $\mu\text{m}$ , a) Impact velocity (m/s), b) Local erosion rates (mg/g)



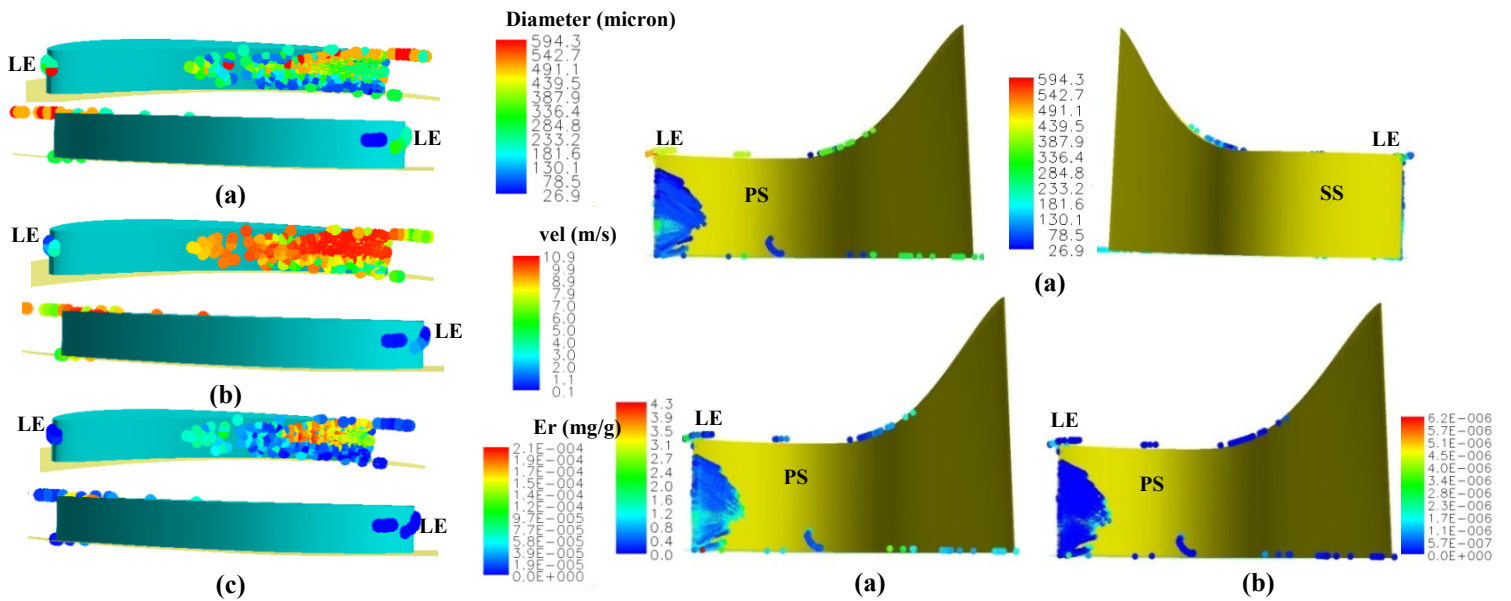
**Figure 17.** Sample of trajectories in vane and rotor for sand particle 1000  $\mu\text{m}$ , when operating at 1900 rpm



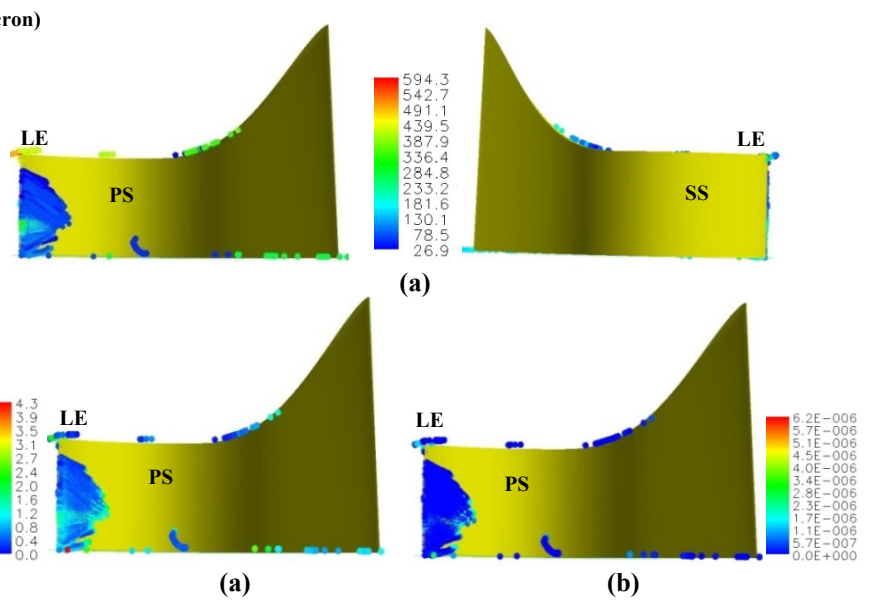
**Figure 18.** Sample of impacts over the vane with particles 1000  $\mu\text{m}$ : a) Impact velocity (m/s), b) Erosion rates (mg/g)



**Figure 19.** Sample of impacts over the rotor blade with particles 1000  $\mu\text{m}$ , a) Impact velocity (m/s), b) Erosion rates (mg/g)

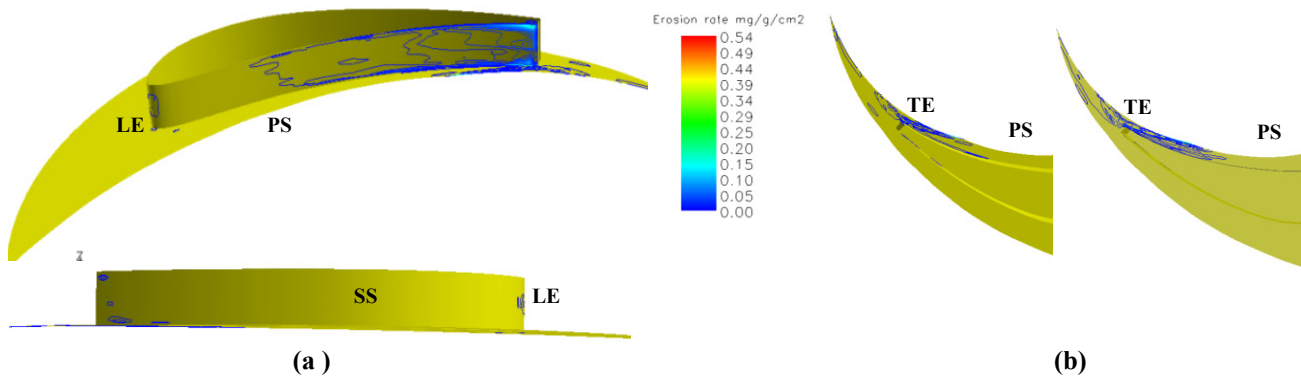


**Figure 20.** Sample of impacts over vane: a) particle size, b) particle velocity (m/s), c) Erosion rates (mg/g)

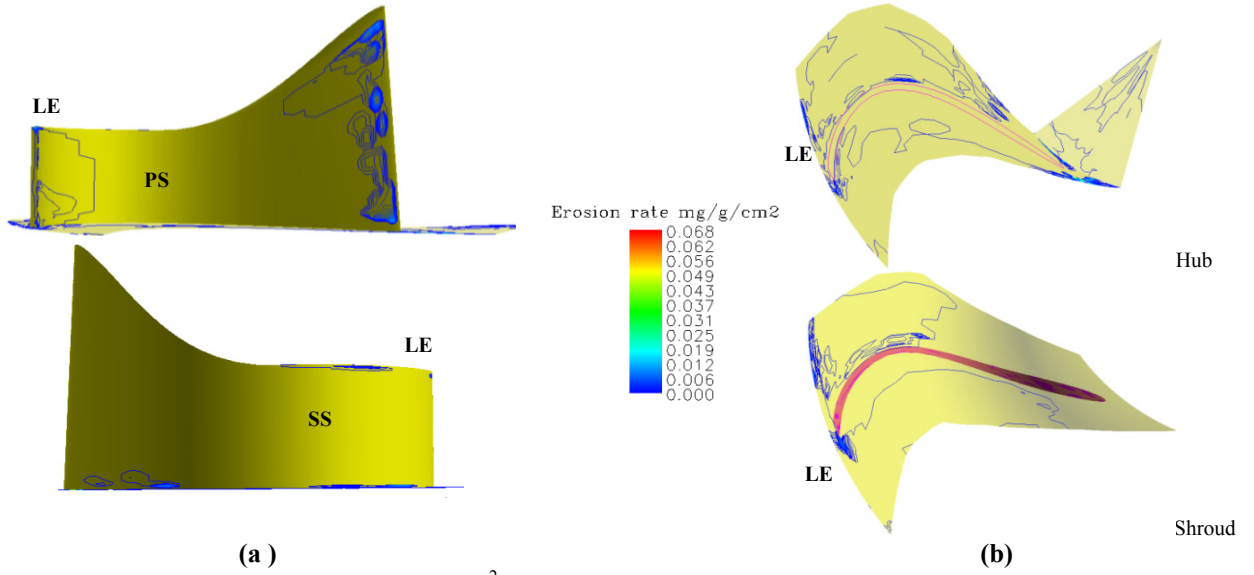


**Figure 21.** Sample of impacts over rotor blade, particles 10-1000  $\mu\text{m}$ : a) Impact diameter, b) Impact velocity (m/s), c) Erosion rates (mg/g)

The results obtained when simulating sand particles (10-1000  $\mu\text{m}$ ) ingestion at an extreme concentration of 1000  $\text{mg}/\text{m}^3$  show that the vane is more affected by erosion due to the relatively higher absolute velocity and acceleration imparted on particles. The inlet region of the runner has highest absolute velocity but small relative velocity, hence the impact of kinetic energy is small compared to force exerted by large accelerating particle. Contrary to that, the relative velocity is highest at the outlet of runner. Indeed, the contours of predicted equivalent erosion rates ( $\text{mg}/\text{g}/\text{mm}^2$ ) in the vane reveal high levels found over the pressure side near trailing edge and towards root and tip, which are attributed to the crowded particles in this region, producing high frequencies of impacts at relatively higher velocities. Indeed, as revealed from Fig. 22.a, there are two regions of extreme erosion reaching an equivalent rate of 0.54  $\text{mg}/\text{g}/\text{mm}^2$  observed toward the trailing edge around the tip and root corners, which are attributed to high impact velocities and impingement angles close to the optimum erosion angle, in addition to the secondary flows affecting small size particles. These two clear spots of erosion at the top and bottom of trailing edge are the critical regions where this vane might fail. Also, the shroud of vane suffers from erosion (Fig. 22.b) at the aft from pressure side and along wake, in addition to spots of erosion attributed in some extent to particles impacts after rebounding off from the rotor blade. When a Francis turbine manipulates sand laden water, erosion of vane may be attributed in some extent to the turbulence erosion related to the fine grain sand, whereas the secondary flow erosion in the corner between the vane and hub and shroud is due to fine and medium size particles. In addition, it can be attributed to the separation of large particles from the streamlines due to rotation of water in the front of runner, which brings particles to strike the vane surface. The predicted equivalent erosion rates in the rotor blade are presented in Fig. 23.a depicting a spread of erosion around the blade leading edge due to its direct exposure to a dense flux of particles entering at large incidence angles. The critical region of high levels of erosion wear as observed over the leading edge extends to the fore part of pressure side. As this inlet region of runner is sensitive to incorrect pressure distribution between pressure side and suction side, any separation caused by this may cause severe local erosion at the inlet due to fine grain sand. As also noticed from Fig. 23.a, there is a dense region of erosion towards the exducer extending from hub to shroud. The turbulence erosion due to fine sand is always susceptible at the exit of rotor blade, and because of the effect of centrifugal force, most of the particles will move towards the outer diameter of runner and hence more erosion is identified. On the suction side, a strip of erosion wear is observed along the tip, toward the root and from the front and rear junctions of the blade. As depicted in Fig. 23.b, the shroud is eroded mainly at the fore part near the suction side, due to particles centrifugation. On the hub, the erosion spreads around the blade with spots of intense erosion wear at the front and aft blade junctions and following trailing edge wake.



**Figure 22.** Equivalent erosion rates ( $\text{mg}/\text{g}/\text{mm}^2$ ) over the vane, resulting from solid particle 10-1000  $\mu\text{m}$  impacts of a concentration (1000  $\text{mg}/\text{m}^3$ ): a) Pressure side and suction side, b) Hub (right) and shroud (left)

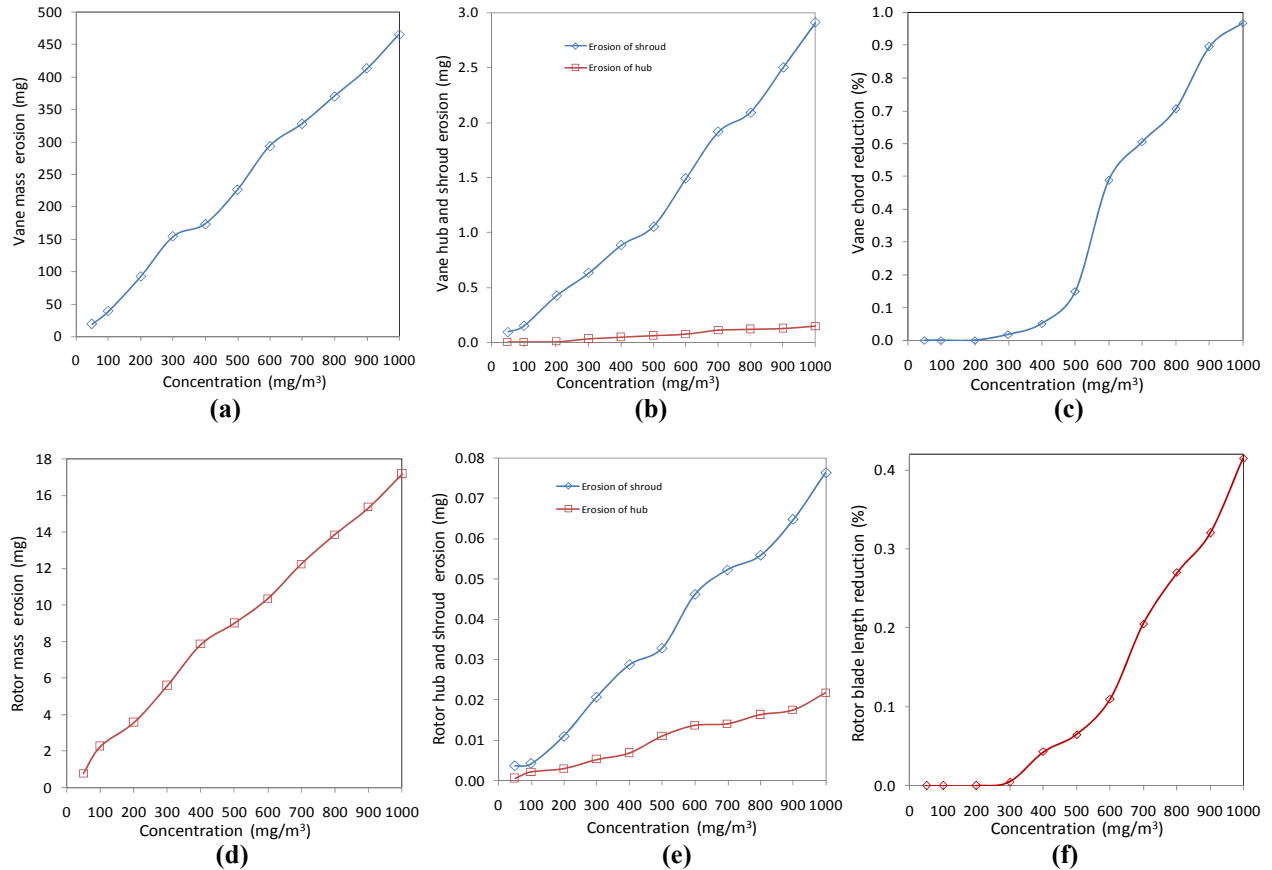


**Figure 23.** Equivalent erosion rates ( $\text{mg/g/mm}^2$ ) over the rotor blade, resulting from solid particle 10-1000  $\mu\text{m}$  impacts of a concentration ( $1000 \text{ mg/m}^3$ ): a) Pressure side and suction side, b) Hub and shroud

The cumulative mass erosion as computed over the different mesh elements led to the determination of the local penetration depths, which served to estimate the new coordinates of the eroded vane and rotor blade. The deterioration of vane is characterized by a variation in the pressure side profile from throat to trailing edge. The increased exit passage area and cavities formation due to material removal will alter the flow directions at rotor blade entry and operating condition of the turbine. The deteriorated rotor blade reveals that the removal of material from the leading edge and trailing edge may affect the stagnation point, incidence, recirculation, pressure distribution and flow direction at exit, which subsequently alter the operating condition of this turbine. Table 1 presents the results of the estimated erosion and geometry deterioration of vane and rotor blade after one week of quartz particle ingestion for a concentration range in between 50-1000  $\text{mg/m}^3$ . The assessed parameters are the mass erosion, overall erosion rate and geometry deterioration estimated as percentages of chord and thickness reduction, as plotted in Fig. 24. It is clear that the material removal and the geometry changes are related to the particle size and concentration and duration of exposure for this operating condition of Francis turbine. According to Tab. 1 the mass erosion of one vane with particle concentration is from 19.047 mg to 464.234 mg, which is well illustrated by Fig. 24.a. Also it is noticed that the overall erosion rate is almost constant (Tab. 1) and has an average value of  $8.2 \times 10^{-3} \text{ mg/g}$ . The mass erosion of the vane's shroud (Fig. 24.b) is so important and varies with concentration from 0.093 mg to 2.911 mg, whereas that of hub is lower i.e. from  $6.50 \times 10^{-4} \text{ mg}$  to 0.144 mg. The average reduction in the vane chord is from  $2.1 \times 10^{-5} \%$  to 0.96% (Tab. 1 and Fig. 24.c), and the thickness from  $2.6 \times 10^{-4} \%$  to  $5.3 \times 10^{-3} \%$ , as seen from Tab.1. The mass erosion of rotor blade is noticeably increasing with concentration (Tab. 1 and Fig. 24.d) from 0.788 mg to 17.176 mg. As noticed, the overall erosion rate is almost constant and has an average around  $3.9 \times 10^{-4} \text{ mg/g}$ . Also, the mass erosion of shroud is found to increase with particle concentration from  $3.65 \times 10^{-3} \text{ mg}$  to  $7.63 \times 10^{-2} \text{ mg}$ , and that of the hub from  $5.72 \times 10^{-4} \text{ mg}$  to  $2.21 \times 10^{-2} \text{ mg}$ , as seen from Fig. 24.e. The erosion phenomenon is shown to distort the leading edge of rotor blade and reduce progressively its thickness and length, as seen from Fig. 24.e. The predicted geometry deterioration with concentration reveals (Fig. 24.f) an average decrease in the blade length from  $4.6 \times 10^{-6} \%$  to 0.415%, and the thickness (Tab. 1) from  $1.4 \times 10^{-4} \%$  to  $3.1 \times 10^{-3} \%$ . These results may help in assessing the lifetime for similar models of Francis turbine.

**Table 1.** Erosion and geometry deterioration due to sand particle ingestion after one week

Erosion parameters		Concentration (mg/m <sup>3</sup> )										
		50	100	200	300	400	500	600	700	800	900	1000
Particle rate (mg/s)		125.98	253.85	503.71	755.06	1016.78	1258.35	1511.78	1796.89	2014.70	2271.71	2531.22
Number of particles per second		2644	5544	10939	16290	22173	27178	32691	39066	43756	49101	54755
Vane	Erosion (mg)	19.047	38.585	91.944	154.022	173.147	225.931	292.963	327.892	369.778	412.395	464.234
	Reduction of blade mass (%)	5.04E-02	0.102	0.243	0.407	0.458	0.598	0.775	0.868	0.979	1.092	1.231
	Overall erosion rate (mg/g)	7.53E-03	7.59E-03	8.79E-03	8.81E-03	7.72E-03	8.26E-03	8.54E-03	8.10E-03	8.53E-03	8.31E-03	8.21E-03
	Chord reduction (%)	2.15E-05	2.59E-05	9.93E-05	1.78E-04	0.051	0.149	0.487	0.605	0.705	0.895	0.967
	Thickness reduction (%)	2.66E-04	5.42E-04	1.29E-03	2.15E-03	2.41E-03	2.90E-03	3.61E-03	3.90E-03	4.29E-03	4.66E-03	5.27E-03
	Erosion of hub (mg)	6.50E-04	1.48E-03	4.72E-03	3.10E-02	0.047	6.15E-02	7.13E-02	0.107	0.119	0.126	0.144
	Erosion of shroud (mg)	0.093	0.147	0.423	0.631	0.885	1.054	1.491	1.915	2.091	2.498	2.911
Rotor Blade	Erosion (mg)	0.788	2.276	3.580	5.598	7.854	9.002	10.335	12.230	13.838	15.348	17.176
	Reduction of blade mass (%)	4.0E-02	0.115	0.181	0.284	0.398	0.456	0.524	0.620	0.702	0.778	0.871
	Overall erosion rate (mg/g)	3.93E-04	4.01E-04	3.99E-04	4.06E-04	4.07E-04	3.90E-04	3.97E-04	4.45E-04	3.904	3.84E-04	3.73E-04
	Blade length reduction (%)	4.66E-06	8.01E-06	1.84E-05	4.86E-03	4.31E-02	6.5E-02	0.110	0.205	0.271	0.324	0.415
	Thickness reduction (%)	1.42E-04	4.10E-04	6.46E-04	1.01E-03	1.42E-03	1.63E-03	1.87E-03	2.31E-03	2.54E-03	2.79E-03	3.07E-03
	Erosion of hub (mg)	5.72E-04	2.10E-03	2.95E-03	5.30E-03	6.90E-03	1.10E-02	1.361E-02	1.41E-02	1.64E-02	1.75E-02	2.17E-02
	Erosion of shroud (mg)	3.65E-03	4.22E-03	1.10E-02	2.07E-02	2.87E-02	3.29E-02	4.61E-02	5.23E-02	5.58E-02	6.47E-02	7.63E-02

**Figure 24.** Erosion degradations after one week of particle ingestion: a) vane blade mass erosion, b) Hub and shroud erosion, c) Length reduction: d) Rotor blade mass erosion, e) Hub and shroud erosion, f) Length reduction

## CONCLUSION

This small Francis water turbine is characterized by complex flow features with a typical large eddy in the runner. These flow details are shown to affect strongly the sand particle trajectory trend in this turbomachinery. The obtained results of erosion patterns show that the vane is more affected by erosion due to relatively higher absolute velocity and acceleration imparted on particles. The dense erosion contours over the last part of pressure side, typically towards the root and tip are

attributed to the high frequencies of impacts. The inlet region of the runner has a smaller relative velocity, hence impact due to kinetic energy is small compared to force exerted by large accelerating particle. The inlet region of runner is sensitive to cumulated local erosion by fine quartz particles. In addition, there is a dense region of erosion at exducer from root to tip, attributed to the effect of centrifugal force forcing most of particles to move towards outer diameter. According to this study, the local velocities of impacts and the subsequent erosion rates are low as compared to those encountered in gas turbines. However, a special surface treatment of the most affected regions is necessary in order to increase the lifetime of the components to prevent risks of erosion.

## REFERENCES

- [1] Sage W and Tilly G.P, 1969, "The Significance of Particles Sizes in Sand Erosion of Small Gas Turbines", JRAeS, Vol 73, May 1969, pp 427-428
- [2] Truscott, G. F., 1970, "A Literature Survey on Abrasive Wear in Hydraulic Machinery", Wear, 20 (1970) 29
- [3] Hussein, M. F., and Tabakoff, W., Computation and Plotting of Solid Particle Flow in Rotating Cascades, Computers and Fluids, Vol. 2, No. 1, 1974, pp. 1–15.
- [4] Elfeki, S. and Tabakoff, W., Erosion Study of Radial Flow Compressor with Splitters, *Journal of Turbomachinery*, Vol 109 January 1987.
- [5] Ghenaiet, A., 2012, "Simulation of Particle Trajectories and Erosion in a Centrifugal Compressor", *ASME Journal of Turbomachinery*, Vol 134, issue 5 September 2012, page 051022 (19 pages),
- [6] Tabakoff, W., and Hamed A, 1988, "Temperature Effect on Particle Dynamics And Erosion in Radial Inflow Turbine", *ASME Journal of turbomachinery*, Vol 110, April 1988, pp 259 –264
- [7] Ghenaiet, A., Tan S. C., and Elder, R. L. 2001, "Particles Trajectories through an Axial Fan and Performance Degradation Due to Sand," ASME/ 2001–GT–0497
- [8] Ghenaiet, A., 2012, "Study of Sand Particle Trajectories and Erosion into the First Compression Stage of a Turbofan", *ASME Journal of Turbomachinery*, Vol 134, issue 5 September 2012, page 051025 (17 pages).
- [9] Ghenaiet, A., 2014, "Study of Particle Ingestion through Two-Stage Gas Turbine", ASME/ IGTI paper GT2014-25759
- [10] Clift, J. R. Grace, and M. E. Weber, *Bubbles, Drops and Particles*, Academic Press, New York, 1978.
- [11] Haider, A. and Levenspiel, O. "Drag Coefficient and Terminal Velocity of Spherical and Non Spherical Particles", *Powder Technology*, 58 (1989) 63.
- [12] Sommerfeld, M. "Theoretical and Experimental Modelling of Particulate Flow - Overview and Fundamentals", VKI Lecture series 2000–06, April 3-7 2000, Von Karman Institute, Belgium
- [13] Haider, A., and Levenspiel, O., 1989, "Drag Coefficient and Terminal Velocity of Spherical and Non Spherical Particles", *J of Powder Technology*, 58 (1989) 63.
- [14] Clark, H., and Burmeister, L., 1992, "The influence of the squeeze film on particle impact velocities in erosion", *Int. J. Impact Eng.*, 12, No. 3, pp.415–426.
- [15] Gosman, A. D., and Ionnides, E., 1981, "Aspects of Computer Simulation of Liquid Fuelled Combustors", 19<sup>th</sup> Aerospace Science Meeting St Louis Missouri, AIAA 81-0323
- [16] Erwin Fehlberg, "Classical Fifth, Sixth, Seventh and Eighth Order RK Formulas with Step Size Control", NASA TR-287 October 1968
- [17] Tabakoff, W., Hamed, A., and Murugan, D. M., "Effect of Target Materials on the Particle Restitution Characteristics for Turbomachinery Application", *Journal of propulsion and power* Vol. 12 No2, March-April 1996
- [18] Finnie, I., 1960, "Erosion of Surfaces by Solid Particles", *Wear*, vol 3 1960 pp 87-103
- [19] Goodwin, J. E, Sage, W. and Tilly G. P., 1984, " Study of Erosion by Solid Particles ", *Proceeding of the Institution of Mechanical Engineers*, vol 1984 pt 10 N<sup>o</sup> 15 1970, pp 279-292
- [20] Rao, P. V. and Buckley, D. H., 1985, "Characterisation of Solid Particle Erosion Resistance of Ductile Metals Based on Their Properties", *ASME Journal of Engineering for Gas Turbine and Power*, Vol 107, 1985, pp 669- 678
- [21] Grant, G. and Tabakoff, W., 1974, " Erosion Prediction in Turbomachinery Due to Environmental Solid Particles ", AIAA Paper No 74-16 AIAA 12th Aerospace Sciences Meeting Washington DC/ Jan 30- Feb1, 1974
- [22] Balan, C. and Tabakoff, W., 1984, "Axial Flow Compressor Performance Deterioration", AIAA paper 84 -1208, June 1984